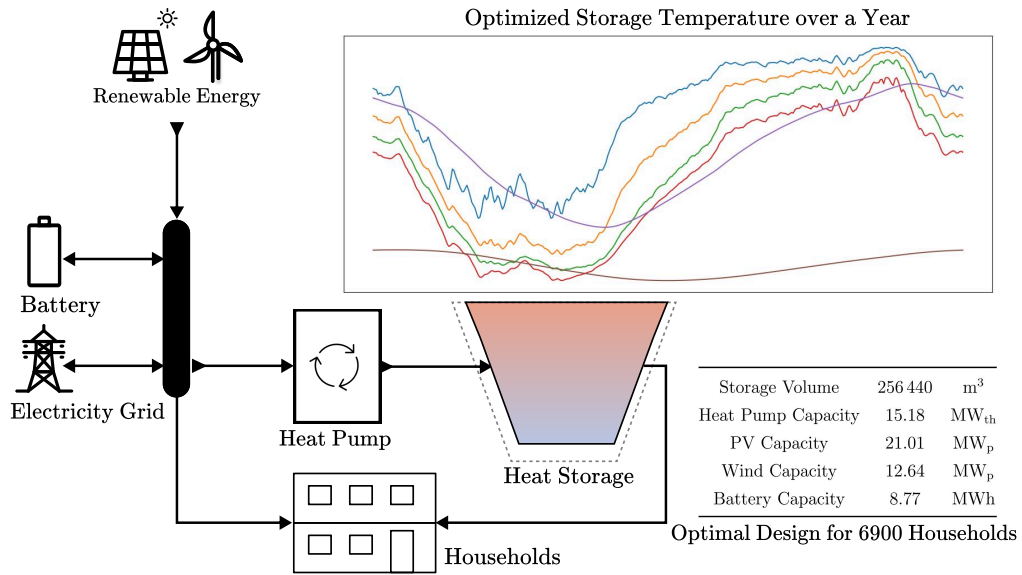


Graphical Abstract

Numerical Method for Simultaneous Design and Control Optimization of Seasonal Thermal Energy Storage Systems

Wonsun Song, Jakob Harzer, Christopher Jung, Leon Sander, Moritz Diehl



Highlights

Numerical Method for Simultaneous Design and Control Optimization of Seasonal Thermal Energy Storage Systems

Wonsun Song, Jakob Harzer, Christopher Jung, Leon Sander, Moritz Diehl

- Optimal control problem formulation for design and control of multi-energy systems.
- Stratified underground thermal energy storage model using a lumped-parameter method.
- Computational complexity reduction using the averaging method.
- Economically viable pathway to carbon-neutral energy systems.

Numerical Method for Simultaneous Design and Control Optimization of Seasonal Thermal Energy Storage Systems

Wonsun Song^a, Jakob Harzer^a, Christopher Jung^b, Leon Sander^b, Moritz Diehl^{a,c}

^a*Department of Microsystems Engineering (IMTEK), University of Freiburg, 79110, Freiburg, Germany*

^b*Department of Environmental Meteorology, University of Freiburg, 79085, Freiburg, Germany*

^c*Department of Mathematics, University of Freiburg, 79104, Freiburg, Germany*

Abstract

The transition to a carbon-neutral energy system requires massive installation of renewable energy sources and economically feasible energy storage solutions. This study addresses these challenges by optimizing the design and control strategies of an energy system that meets the heat and electricity demands of a community. The proposed system integrates solar and wind power with energy storage, including seasonal thermal energy storage (STES) and battery, coupled via a heat pump. This approach enhances self-sufficiency and effectively mitigates seasonal mismatches. To model heat transfer between the storage and the ground in the STES system, we employ a multi-node lumped-parameter method. The optimization problem is formulated as a periodic optimal control problem, which is then transcribed into a nonlinear programming problem. To reduce computational complexity, we apply the averaging method, which significantly lowers the effort required to solve the problem. We apply this approach to a case study, where the economically optimized configuration results in a projected total energy cost per household of approximately 75 €/month over 30 years for both heat and electricity. This study demonstrates the feasibility of designing economically viable, autonomous energy communities in real-world scenarios, and provides a comprehensive optimization framework for designing system components and control strategies.

Keywords: Energy Transition, Renewable Energy, Seasonal Thermal Energy Storage, Sector Coupling, Optimal Control, Averaging Method

Abbreviations

OCP	Optimal Control Problem
NLP	Non-Linear Programming Problem
STES	Seasonal Thermal Energy Storage
UTES	Underground Thermal Energy Storage
PTES	Pit Thermal Energy Storage
PV	Photovoltaics
HP	Heat Pump
COP	Coefficient of Performance
SOC	State of Charge
ANI	Annuity of the Investment
ANF	Annuity Factor
CAPEX	Capital Expenditures
OPEX	Operational Expenditures
MAPE	Mean Absolute Percentage Error
RMLSE	Root Mean Square Logarithmic Error
SH	Space Heating
DHW	Domestic Hot water

Optimization Symbol

x	State (-)
u	Control (-)
s	Scaling factor (-)
θ	Parameter vector (-)
h	Step size (-)
t	Time (s)
N_c, N_f	Number of Coarse, Fine discretization Points (-)
n	Number of variables (-)

Heat Transfer Symbol

λ	Thermal conductivity (W/(m K))
\dot{Q}	Heat Transfer Rate (W)
P	Power (W)
U	Overall heat transfer coefficient (W/(m ² K))
R	Thermal resistance (K/W)
C_s, C_g	Thermal capacitance (J/K)
c_p	Specific heat capacity (J/(kg K))

T	Temperature (K)
\dot{T}	Rate of temperature change (K/s)
\dot{m}	Mass flow rate (kg/s)
M	Number of storage layer (-)
N	Number of ground layer (-)
V	Volume (m ³)
A	Area (m ²)
z	Storage height (m)
d	Ground distance (m)
η	Efficiency (-)
ρ	Density (kg/m ³)

Miscellaneous Symbol

I	Investment Cost (€)
c	Price (€/kWh)
n	Years (-)
r	Interest rate (%)
C	Installed capacity (W or Wh)

Indices

f	Fine
c	Coarse
re	Renewable Energy
b	Battery
ch	Charging
dis	Discharging
s	Storage
g	Ground
bc	Boundary Condition
el	Electricity
hh	Households
sup	Supply
ret	Return
eff	Effective
top	Top layer
amb	Ambient
q	Cross-sectional
surf	Surface

1. Introduction

Climate change, driven by anthropogenic greenhouse gas emissions, is one of the greatest challenges that human society is facing today. The energy sector, accounting for three-quarters of total emissions and relying on fossil fuels for 80% of global energy, plays a pivotal role in the transition to a sustainable future [1]. A major obstacle in this transition is the inherent variability of renewable energy sources, which requires storage solutions. While batteries effectively manage short-term fluctuations, addressing seasonal mismatches requires long-term storage. Hydrogen storage shows potential; however, its application with renewable electricity remains economically unfeasible [2]. In contrast, Underground Thermal Energy Storage (UTES) has emerged as a mature, cost-effective technology, particularly suited for long-term applications [3].

This study focuses on practical and economically viable solutions for achieving carbon neutrality, considering realistic pricing schemes. We propose an energy system that combines photovoltaics and wind energy together with storage solutions, including UTES and short-term battery storage, coupled via a heat pump. The generated and stored electricity, combined with stored heat, meets the community's electricity and heating demands. Among the various UTES technologies, this study focuses on Pit Thermal Energy Storage (PTES), which involves excavating a large, water-filled pit. PTES offers an excellent balance of flexibility, cost-effectiveness, and scalability, making it ideal for large-scale storage applications [3]. Its high charging and discharging rates make it particularly advantageous for cross-sectoral systems. Residual energy imbalances—whether excess or deficits—are managed through the electricity grid, with an emphasis on minimizing dependency on it. Given this system, two key questions arise:

1. For a given demand profile over a year, how should we control the energy flows?
2. How should the system components be sized to minimize the running and investment costs?

We tackle these questions by formulating and solving one single, large non-

linear optimization problem:

$$\begin{array}{ll} \text{minimize} & \text{(Total Cost)} \\ \text{(control strategy)} & \\ \text{(design parameters)} & \end{array} \quad (1a)$$

$$\text{subject to} \quad \text{(year-periodic state simulation),} \quad (1b)$$

$$\text{(operational constraints),} \quad (1c)$$

$$\text{(demand satisfaction)} \quad (1d)$$

1.1. Related Work

Mathematical modeling of pit thermal energy storage (PTES) has been extensively studied, with many approaches employing partial differential equations solved using tools like COMSOL [4] and TRNSYS [5]. COMSOL, which relies on the finite element method, is computationally intensive and ill-suited for optimization tasks involving PTES and renewable energy systems. In contrast, TRNSYS employs a coarse-resolution model that allows system integration but focuses primarily on simulation rather than seamless integration into optimization algorithms. Moreover, both tools are proprietary, restricting source code access and limiting opportunities for customization and advanced optimization. For a comprehensive review of modeling approaches, we refer the reader to [6, 7].

Simpler modeling approaches have been proposed to address the computational challenges of long-term optimization. For example, Kotzur et al. [8] proposed a time-series aggregation method to reduce computational complexity and used a simplified state-of-charge equation for storage. Platforms like the Energy Hub Design Optimization (EHDO) framework [9] focuses on yearly energy system optimization, determining component sizes such as storage and generation capacities through mixed integer linear programming. However, these models often oversimplify heat storage dynamics, typically assuming a fully mixed storage model with a single temperature node. This simplification inadequately captures the mass flow and temperature stratification required for accurate heat storage modeling.

To balance computational efficiency with modeling accuracy, we adopt a multi-node lumped-parameter method. This approach captures key dynamics, including temperature stratification and mass flow effects in the storage and underground environment, while remaining computationally feasible for long-horizon optimization. Furthermore, we provide our method as open-source, enabling broader adoption and customization.

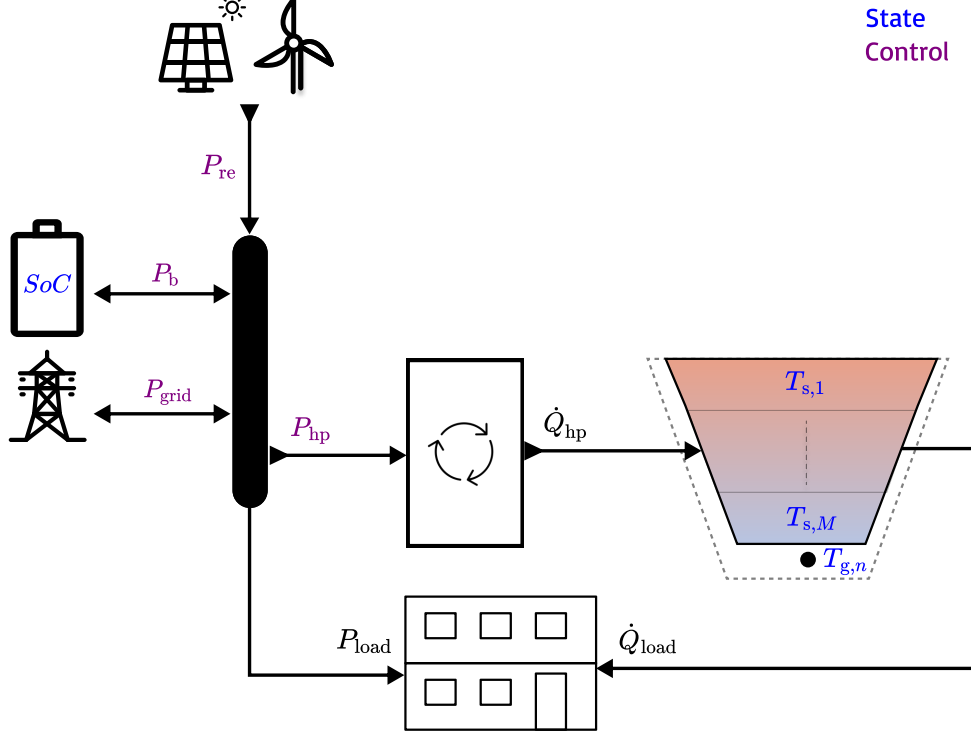
Given these considerations, we formulate and solve an optimal control problem (OCP) to determine optimal design parameters and control strate-

gies for the proposed system. Solution strategies for OCP are broadly categorized into indirect and direct methods. Indirect methods, which follow a “first optimize, then discretize” philosophy, require deriving first-order necessary conditions and solving a boundary value problem [10]. In contrast, direct methods discretize state and control trajectories first, transforming the problem into a finite-dimensional nonlinear programming problem (NLP). This approach simplifies the handling of state constraints and inequalities. For this work, we apply a direct method known as the “multiple shooting” technique. This method introduces variables, referred to as “shooting nodes,” to approximate state trajectories on a time grid. Consistency between these nodes is enforced using constraints derived from the system dynamics. For more details on transcribing OCP with direct methods and solving the resulting NLPs, we refer the reader to [10, 11, 12].

1.2. Contribution

This paper combines four key concepts:

1. Advanced yet optimization-friendly thermal energy storage modeling: We develop a stratified underground thermal energy storage model based on a multi-node lumped-parameter method. This approach captures essential dynamics, such as temperature stratification and mass flow, while incorporating interactions with the surrounding ground. It ensures computational efficiency and differentiability, making it suitable for long-horizon optimization problems.
2. Formulation of a periodic optimal control problem (OCP): We introduce a novel OCP framework that optimizes design parameters (e.g., installed capacities of renewable energy sources, storage, and batteries) and operational strategies.
3. Reduction of computational complexity: To address the computational challenges associated with long-horizon optimization problems, we apply an averaging method to reduce computational complexity while preserving the accuracy needed for reliable solutions.
4. Economically feasible carbon-neutral energy systems: Through a case study of the Dietenbach district in Freiburg, Germany, we demonstrate the practical and economic feasibility of achieving carbon neutrality. The proposed system integrates renewable energy sources, and energy storage, providing a replicable model for sustainable energy systems at the district level.



State
Control

Figure 1: System overview

2. System Model

This chapter provides a mathematical description of the system used in the optimal control problem. The proposed system is sketched in Figure 1. We explain the details of each component in the following subsections.

2.1. Electric Power Balance

The electric power balance ensures that the total electricity input equals the total usage at each time step. Mathematically, this balance can be expressed as:

$$P_{re}(t) - P_{load}(t) - P_{hp}(t) - P_b(t) + P_{grid}(t) = 0 \quad (2)$$

where

$$P_{re}(t) = s_{pv}P_{pv,0}(t) + s_{wind}P_{wind,0}(t) \geq 0 \quad (3)$$

represents the renewable power generation. Here, $P_{pv,0}(t)$ and $P_{wind,0}(t)$ are the known power profiles of photovoltaic (PV) and wind generation

considering the default installed capacities $C_{pv,0}$, $C_{wind,0}$, respectively. These default installed capacities, scaled by respective design parameters s_{pv} and s_{wind} , result in $C_{pv} = s_{pv}C_{pv,0}$, $C_{wind} = s_{wind}C_{wind,0}$. The battery power, $P_b(t)$, consists of charging $P_b^+(t)$ and discharging $P_b^-(t)$ variables, such that $P_b(t) = P_b^+(t) - P_b^-(t)$. Similarly, grid power exchange, $P_{grid}(t)$, is split into import $P_{grid}^+(t)$ and export $P_{grid}^-(t)$, expressed as $P_{grid}(t) = P_{grid}^+(t) - P_{grid}^-(t)$. The electricity demand profile $P_{load}(t)$ is treated as a known profile. All power variables are constrained to be non-negative:

$$0 \leq (P_b^+(t), P_b^-(t), P_{grid}^+(t), P_{grid}^-(t), P_{hp}(t)) \quad (4)$$

2.2. Battery Model

The state of charge (SOC) of the battery, denoted $x^b(t) \in [0, 1]$, evolves according to:

$$\dot{x}^b(t) = f^b(P_b^+(t), P_b^-(t); s_b) = \frac{1}{C_b} \left(P_b^+(t) \cdot \eta_{ch} - \frac{P_b^-(t)}{\eta_{dis}} \right) \quad (5)$$

Here, C_b is the battery capacity in Wh, is scaled by s_b based on a default capacity $C_{b,0}$. η_{ch} , η_{dis} are the charging and discharging efficiencies, respectively, both assumed at 0.95. The SOC is constrained between 0 and 1:

$$0 \leq x^b(t) \leq 1 \quad (6)$$

The charging and discharging power is limited to one-fourth of the total capacity per time step, corresponding to a 0.25C rate:

$$0 \leq P_b^+(t) \leq C_b/4 \text{ h}, \quad (7a)$$

$$0 \leq P_b^-(t) \leq C_b/4 \text{ h} \quad (7b)$$

This model excludes detailed dynamics such as efficiency variations, self-discharge rates, and state-of-health degradation, as the primary focus of this paper is on seasonal thermal energy storage. For more comprehensive battery models, we refer the reader to [13].

2.3. Heat Pump Model

The heat pump uses surplus renewable electricity to elevate the temperature of thermal energy storage rather than direct heating for households. The coefficient of performance (COP) of the heat pump is:

$$\text{COP} = \eta_{\text{Lorenz}} \cdot \frac{T_{\text{sink}}}{T_{\text{sink}} - T_{\text{source}}} \quad (8)$$

where η_{Lorenz} is the Lorenz efficiency factor, set to 0.5 in this study to reflect industrial-scale heat pump performance [14]. T_{source} corresponds to the ambient temperature $T_{\text{amb}}(t)$, and the sink temperature is fixed at 86°C . Now the heat transfer rate \dot{Q}_{hp} , is calculated as:

$$\dot{Q}_{\text{hp}}(t) = \text{COP}(t) \cdot P_{\text{hp}}(t) \quad (9)$$

Heat pump's maximum capacity, defined as $C_{\text{hp}} = s_{\text{hp}} \cdot C_{\text{hp},0}$, where s_{hp} is a scaling parameter relative to the default capacity $C_{\text{hp},0}$. The heat transfer rate is constrained by C_{hp} :

$$0 \leq \dot{Q}_{\text{hp}}(t) \leq C_{\text{hp}} \quad (10)$$

This study focuses on air-source heat pumps due to their practical implementation advantages. Their performance improves in warmer summer conditions, making them especially well-suited for integration with PV generation and seasonal storage during the summer season. The heat pump model does not account for startup dynamics, ramp-up times, or additional electrical power requirements.

2.4. Thermal Energy Storage Model and Heating System

In the model for the Pit Thermal Energy Storage (PTES), we neglect the effects of groundwater flow (convective heat transfer in the ground) and focus solely on heat conduction. The transient conduction process is simplified using a multi-node lumped-parameter approach, also known as the computational capacity resistance model (CaRM), which draws an analogy to electric circuits [15]. The concepts behind this model are illustrated in Figure 2, which shows the heat transfer between the storage layers and the ground. Figure 3 depicts the storage and ground behavior along with the thermal exchange between them. Each dotted line represents a different ground layer, spaced equally. Temperatures are indicated at the center of each layer. Heat is injected into and supplied from the top storage layer, while the return flow is directed to the bottom layer.

The geometry of the storage is a truncated pyramid, with square top and bottom faces of differing areas. Considering the district's heating demand, the default storage volume is set to $200\,000\text{ m}^3$. This volume is scaled by the factor s_s to determine the optimized dimensions of the top and bottom faces. Initially, a side length of the top and bottom faces are 153.3 m and 73.2 m, respectively. The storage height is fixed at 15 m, as this is a common choice for pit storage due to excavation cost constraints. The underground

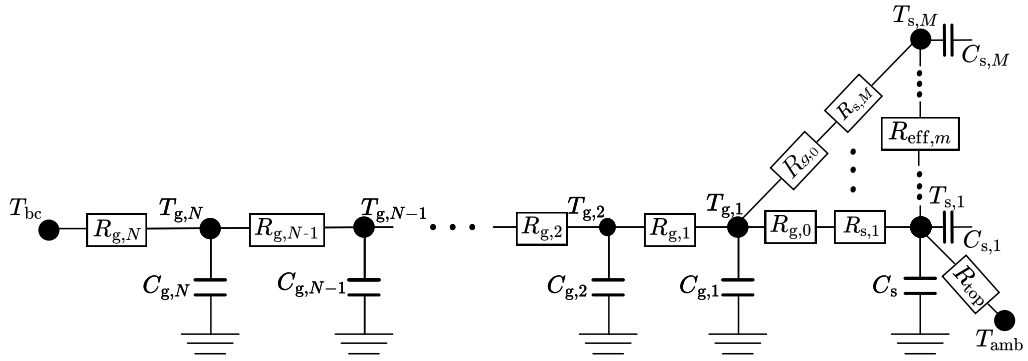


Figure 2: Electric circuit analogy of heat transfer between heat storage and ground

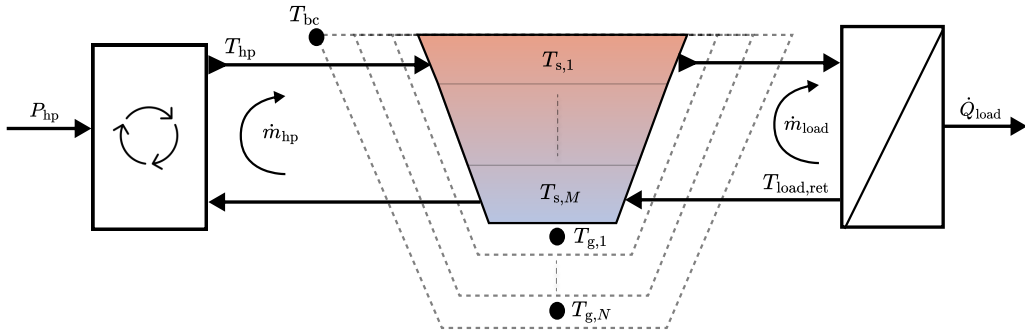


Figure 3: Schematic representation of the pit storage model

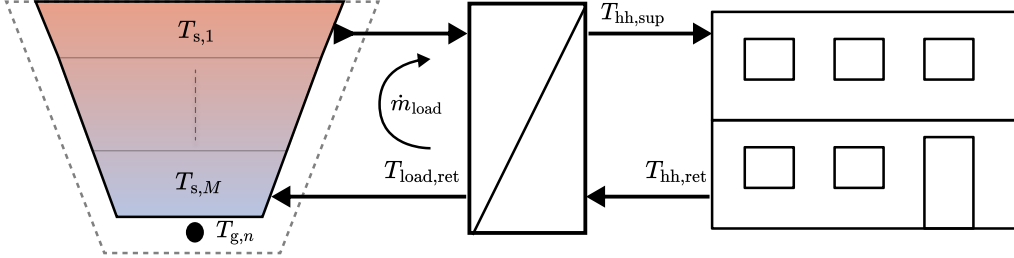


Figure 4: Schematic representation of the heating supply and return flows in the system

geometry is approximated with planar walls, introducing inaccuracies at the edges; however, these are neglected in the model. For boundary conditions, we assume a uniform ground temperature of $13.5\text{ }^\circ\text{C}$, based on the relatively stable temperatures observed at depths of 5 m to 10 m in the Freiburg region. More details of the geometry of the storage can be found in [6].

Figure 4 illustrates the flow of heating supply to households and the corresponding return flow. The supply and return temperatures for the household heating demand denoted as $T_{hh,sup}$ and $T_{hh,ret}$, are set to $40\text{ }^\circ\text{C}$ and $20\text{ }^\circ\text{C}$, respectively. These values align with the efficiency goals of the low-temperature, 4th-generation district heating system [16]. For simplicity, we assume a constant temperature difference of 20 K between the supply and return flows. Thus, the return temperature of the heating load is consistently calculated as ($T_{load,ret} = T_{s,1} - 20\text{ K}$), assuming no heat exchange losses and a uniform heat transfer medium. This assumption simplifies the mass flow rate calculations, making $\dot{m}_{load}(t) = \frac{\dot{Q}_{load}(t)}{c_p \cdot 20\text{ K}}$, which depends solely on $\dot{Q}_{load}(t)$.

The storage temperature dynamics are governed by:

$$\begin{aligned} \dot{T}_{s,1} = & \frac{1}{C_{s,1}} \left(c_p \cdot \dot{m}_{\text{hp}}(t)(T_{\text{hp}} - T_{s,1}) + c_p \cdot \dot{m}_{\text{load}}(t)(T_{s,2} - T_{s,1}) \right. \\ & \left. + \frac{T_{s,2} - T_{s,1}}{R_{\text{eff},1}} + \frac{T_{\text{amb}}(t) - T_{s,1}}{R_{\text{top}}} + \frac{T_{g,1} - T_{s,1}}{R_{g,0} + R_{s,1}} \right), \end{aligned} \quad (11a)$$

$$\begin{aligned} \dot{T}_{s,m} = & \frac{1}{C_{s,m}} \left(c_p \cdot \dot{m}_{\text{hp}}(t)(T_{s,m-1} - T_{s,m}) + c_p \cdot \dot{m}_{\text{load}}(t)(T_{s,m+1} - T_{s,m}) \right. \\ & \left. + \frac{T_{s,m-1} - 2T_{s,m} + T_{s,m+1}}{R_{\text{eff},m}} + \frac{T_{g,1} - T_{s,m}}{R_{g,0} + R_{s,m}} \right), \quad \forall m = 2, \dots, M-1, \end{aligned} \quad (11b)$$

$$\begin{aligned} \dot{T}_{s,M} = & \frac{1}{C_{s,M}} \left(c_p \cdot \dot{m}_{\text{hp}}(t)(T_{s,M-1} - T_{s,M}) + c_p \cdot \dot{m}_{\text{load}}(t)(T_{\text{load,ret}} - T_{s,M}) \right. \\ & \left. + \frac{T_{s,M-1} - T_{s,M}}{R_{\text{eff},M}} + \frac{T_{g,1} - T_{s,M}}{R_{g,0} + R_{s,M}} \right), \end{aligned} \quad (11c)$$

where

$$\begin{aligned} C_{s,m} = \rho c_p V_{s,m}, \quad \dot{m}_{\text{hp}}(t) = \frac{\dot{Q}_{\text{hp}}(t)}{c_p(T_{\text{hp}} - T_{s,M})}, \quad R_{s,m} = \frac{1}{U \cdot A_{\text{surf},m}}, \\ R_{\text{eff},m} = \frac{z_m}{\lambda_{\text{eff}} \cdot A_{q,m}}, \quad R_{g,0} = M \cdot R_{g,0,\text{original}}, \quad R_{\text{top}} = \frac{1}{U_{\text{top}} \cdot A_{\text{top}}}. \end{aligned} \quad (12)$$

Here, $C_{s,m}$ represents the thermal capacitance (in J/K) of each discretized section, calculated for a volume $V_{s,m}$, where all sections are divided into equal volumes. The stratified model accounts for forced convection due to $\dot{m}_{\text{hp}}(t)$ and $\dot{m}_{\text{load}}(t)$, and heat transfer between storage layers. The effective thermal resistance $R_{\text{eff},m}$ is determined by the thermal conductivity λ_{eff} , the height z_m of the m -th layer, and its cross-sectional area $A_{q,m}$, assuming equal layer volumes. The thermal resistance $R_{s,m}$ accounts for the effective storage area for each layer, excluding the top layer, as it is insulated to minimize heat loss, while underground layers are uninsulated to leverage the ground heat. Heat transfer between storage and ground layers is represented by $R_{g,0}$, adjusted for the number of layers M due to their parallel connection. More details on the stratified model are provided in

Table 2: Parameters for the storage and underground model

Parameter	Value	Unit
ρ	1000	kg/m ³
c_p	4200	J/(kg·K)
ρ_g	2000	kg/m ³
$c_{p,g}$	700	J/(kg·K)
λ_g	0.47	W/(m·K)
λ_{eff}	0.644	W/(m·K)
U_{top}	0.186	W/(m ² ·K)
U	80	W/(m ² ·K)

[17]. The ground dynamics are modeled as:

$$\dot{T}_{g,1} = \frac{1}{C_{g,1}} \left(\frac{T_{s,1} - T_{g,1}}{R_{g,0} + R_{s,1}} + \dots + \frac{T_{s,M} - T_{g,1}}{R_{g,0} + R_{s,M}} + \frac{T_{g,2} - T_{g,1}}{R_{g,1}} \right), \quad (13a)$$

$$\dot{T}_{g,n} = \frac{1}{C_{g,n}} \left(\frac{T_{g,n-1} - T_{g,n}}{R_{g,n-1}} + \frac{T_{g,n+1} - T_{g,n}}{R_{g,n}} \right), \forall n = 2, \dots, N-1, \quad (13b)$$

$$\dot{T}_{g,N} = \frac{1}{C_{g,N}} \left(\frac{T_{g,N-1} - T_{g,N}}{R_{g,N-1}} + \frac{T_{bc} - T_{g,N}}{R_{g,N}} \right), \quad (13c)$$

where

$$C_{g,n} = \rho_g \cdot c_g \cdot V_n, \quad R_{g,n} = \frac{d_n}{\lambda_g \cdot A_{\text{surf},n}}, \quad (14)$$

represent the thermal capacitance and resistance of the ground layers. Parameters for these dynamics are based on the PTES system in Dronninglund, Denmark [6], and are listed in Table 2. While temperature dynamics (\dot{T}) and parameters such as thermal resistance (R) and capacitance (C) depend on the scaling factor (s_s), these dependencies are omitted in the equations for simplicity.

To achieve a balance between accuracy and computational efficiency, the spatial discretization of the storage is defined by four stratification layers ($m = 4$) for the interior of the storage, along with two ground layers ($n = 2$) separated by a total distance of 4 m, based on simulations in Appendix A.4.

We summarize the storage (including ground) temperatures with the state vector:

$$x^s = (T_{s,1}, \dots, T_{s,M}, T_{g,1}, \dots, T_{g,N})^\top \in \mathbb{R}^{N+M} \quad (15)$$

and the dynamics (11) and (13) as:

$$\dot{x}^s = f^s(x^s, t; s_s) \quad (16)$$

The storage dynamics f^s are time-dependent and influenced by $\dot{Q}_{\text{hp}}(t)$, $\dot{Q}_{\text{load}}(t)$, and $T_{\text{amb}}(t)$ with an affine dependence. Thus, we rewrite the dynamics as:

$$f^s(x^s, t; s_s) = f^s(x^s, \dot{Q}_{\text{hp}}(t), \dot{Q}_{\text{load}}(t), T_{\text{amb}}(t); s_s), \quad (17)$$

as described in Equations (11) to (13).

Storage temperatures are constrained between 10°C and 85°C, with the top storage layer maintaining a minimum temperature of 40°C to meet the district heating network requirements. This can be expressed as:

$$40^\circ\text{C} \leq T_{s,1} \leq 85^\circ\text{C}, \quad (18a)$$

$$10^\circ\text{C} \leq T_{s,m} \leq 85^\circ\text{C}, \quad m = 2, \dots, M \quad (18b)$$

3. Optimal Control Problem in Continuous-Time

In this section, we formulate a periodic optimization problem over a 30-year horizon aimed at minimizing the total cost, which includes both investment and operational costs of the proposed system. The objective is to optimize the design parameters and control strategy, under the assumption that the system operates in a periodic steady state. For simplicity, we consider a repeating cycle extending infinitely over time.

We seek to optimize the fixed design parameters, which include the installed capacities of renewable energy sources, the heat pump, and the length of the storage area:

$$\theta = (s_{\text{pv}}, s_{\text{wind}}, s_{\text{b}}, s_{\text{s}}, s_{\text{hp}}) \in \mathbb{R}^5 \quad (19)$$

Additionally, we aim to optimize the trajectory of the control variables, which consist of the time-dependent power flows:

$$u(t) = (P_{\text{hp}}(t), P_{\text{b}}^+(t), P_{\text{b}}^-(t), P_{\text{grid}}^+(t), P_{\text{grid}}^-(t)) \in \mathbb{R}^5, \quad \forall t \in [0, 365\text{d}] \quad (20)$$

Table 3: Investment parameters, and CAPEX/OPEX of each component¹

	Inv. Cost	Unit	Ref.	CAPEX	OPEX
PV	1491	\$/kW _p	[18]	$I_{pv}C_{pv}$	$0.01 \cdot \text{CAPEX}$
Wind	1569	\$/kW _p	[18]	$I_{wind}C_{wind}$	$0.02 \cdot \text{CAPEX}$
Battery	476	\$/kWh	[18]	$I_b C_b$	$0.02 \cdot \text{CAPEX}$
Storage	30	€/m ³	[19]	$I_s V_s$	$0.01 \cdot \text{CAPEX}$
Heat Pump	375	€/kW	[20]	$I_{hp} C_{hp}$	$0.025 \cdot \text{CAPEX}$
Total				$\text{CAPEX}_{\text{sum}}$	OPEX_{sum}

The state vector $x(t)$ combines the temperatures and the battery's state of charge:

$$x(t) = \begin{bmatrix} x^s(t) \\ x^b(t) \end{bmatrix} \in \mathbb{R}^{M+N+1}, \quad \forall t \in [0, 365\text{d}] \quad (21)$$

The combined dynamics of the system are given by:

$$f(x(t), u(t), t; \theta) = \begin{bmatrix} f^s(x^s(t), \dot{Q}_{hp}(t), \dot{Q}_{load}(t), T_{amb}(t); s_s) \\ f^b(P_b^+(t), P_b^-(t); s_b) \end{bmatrix} \quad (22)$$

Here, $\dot{Q}_{hp}(t) = \dot{Q}_{hp}(P_{hp}(t), T_{amb}(t), t)$ is a function of both the ambient temperature and the control $P_{hp}(t)$, as defined in Equation 9.

Fixed costs are divided into Capital Expenditure (CAPEX) and Operational Expenditure (OPEX), as summarized in Table 3. In this study, we use the annuity method to calculate the annual payment for the CAPEX, ensuring that interest is covered each period and the total CAPEX is fully repaid by the end of the project duration (n years), considering interest rate (r). The relationship between the CAPEX and the annual payment, referred to as the Annuity of the Investment (ANI), is expressed as:

$$\text{CAPEX}_{\text{sum}} = \text{ANI} \cdot \sum_{t=1}^n \frac{1}{(1+r)^t} \quad (23)$$

¹The exchange rate used is 1 \$ corresponding to 0.92 € as the annual average for 2024.

The geometric series can be expressed as:

$$\sum_{t=1}^n \frac{1}{(1+r)^t} = \frac{1 - (1+r)^{-n}}{r} \quad (24)$$

Rearranging to solve for ANI, we obtain:

$$\text{ANI} = \text{CAPEX}_{\text{sum}} \cdot \frac{r(1+r)^n}{(1+r)^n - 1} \quad (25)$$

The term $\frac{r(1+r)^n}{(1+r)^n - 1}$ is known as the Annuity Factor (ANF). For this study, we use $n = 30$ years and $r = 4\%$. The fixed cost is then formulated as:

$$J_{\text{fix}}(\theta) = \text{ANI} + \text{OPEX}_{\text{sum}} \quad (26)$$

The running cost is determined by electricity consumption from the grid and feed-in revenue:

$$J_{\text{run}}(u(t)) = c_{\text{el,buy}} P_{\text{grid}}^+(t) - c_{\text{el,sell}} P_{\text{grid}}^-(t) \quad (27)$$

where $c_{\text{el,buy}}$ and $c_{\text{el,sell}}$ represent the electricity purchase price (30 ct/kWh) and feed-in tariff (1 ct/kWh), respectively. While feed-in tariffs are expected to decrease with the expansion of renewable energy deployment—and we aim to avoid overly large renewable installations solely for feeding electricity into the grid—we maintain a high electricity purchase price to promote grid independence. We summarize the continuous-time optimal control problem as:

$$\underset{x(\cdot), u(\cdot), \theta}{\text{minimize}} \quad \int_0^{365 \text{ d}} J_{\text{run}}(u(t)) dt \quad + \quad J_{\text{fix}}(\theta) \quad (28a)$$

$$\text{subject to} \quad 0 = x(0) - x(365 \text{ d}), \quad (28b)$$

$$\dot{x}(t) = f(x(t), u(t), t, \theta) \quad \forall t \in [0, 365 \text{ d}], \quad (28c)$$

$$0 \geq h(u(t), t, \theta) \quad \forall t \in [0, 365 \text{ d}], \quad (28d)$$

$$0 = g(u(t), t, \theta) \quad \forall t \in [0, 365 \text{ d}], \quad (28e)$$

$$x_{\text{min}} \leq x(t) \leq x_{\text{max}} \quad \forall t \in [0, 365 \text{ d}], \quad (28f)$$

$$u_{\text{min}} \leq u(t) \leq u_{\text{max}} \quad \forall t \in [0, 365 \text{ d}], \quad (28g)$$

$$\theta_{\text{min}} \leq \theta \leq \theta_{\text{max}} \quad (28h)$$

Here, Equation (28b) is a periodicity constraint on the state trajectory. The inequality constraints (28d) consist of the parameter-dependent constraints

(7) and (10), while the only equality constraint (28e) is given by the power balance (2). The state bounds (28f) are defined by equations (18), and (6), while the control bounds (28g) are given by Equation (4). The parameter vectors are bounded in (28h), ranging from $\theta_{\min} = 0.1$ to $\theta_{\max} = 10$, to ensure better convergence and avoid numerical errors.

4. Discretization and NLP Formulation

To numerically solve the optimal control problem (28), we transcribe it into a nonlinear programming problem (NLP) by discretizing the continuous control and state trajectories. We divide the time horizon $t \in [0, 365 \text{ d}]$ into N_f equidistant intervals, with a step size of $h_f = 365 \text{ d}/N_f$, and grid node times $t_k = h_f k, k = 0, \dots, N_f - 1$, such that

$$0 = t_0 \leq t_1 \leq \dots \leq t_k \leq \dots \leq t_{N_f-1} \leq t_{N_f} = 365 \text{ d} \quad (29)$$

where we typically select $N_f = 365 \cdot 24 = 8760$, which corresponds to an hourly grid. We refer to this grid as the “fine” grid and will introduce the “coarse” grid later.

We discretize the problem (28) using multiple shooting, introducing the shooting nodes $x_0, x_1, \dots, x_{N_f} \in \mathbb{R}^{n_x}, x_k = (x_k^s, x_k^b)$ that approximate the state at the grid nodes as $x(t_k) \approx x_k$. The control variables $u_0, u_1, \dots, u_{N_f-1}$ parameterize the control as piecewise constant: $u(t) = u_k \in \mathbb{R}^{n_u} \forall t \in [t_k, t_{k+1})$. Additionally, we treat the following quantities as constant over each grid interval:

$$\begin{bmatrix} T_{\text{amb}}(t) \\ P_{\text{pv}}(t) \\ P_{\text{wind}}(t) \\ P_{\text{load}}(t) \\ \dot{Q}_{\text{load}}(t) \end{bmatrix} = \begin{bmatrix} T_{\text{amb},k} \\ P_{\text{pv},k} \\ P_{\text{wind},k} \\ P_{\text{load},k} \\ \dot{Q}_{\text{load},k} \end{bmatrix}, \quad \forall t \in [t_k, t_{k+1}) \quad (30)$$

The values of the parameters are provided from external data sources; further details can be found in Appendix A. Here, we use one of the simplest possible numerical integration methods for the multiple shooting interval, one single step of an implicit Euler integrator, which proved to be the most efficient choice for our application. Note that more elaborate higher-order integrators exist and could prove to be more efficient on other applications. The system dynamics are then approximated as follows:

$$0 = x_{k+1}^s - x_k^s - h_f f^s(x_{k+1}^s, u_k, t_k, \theta), \quad k = 0, 1, \dots, N_f - 1 \quad (31)$$

$$0 = x_{k+1}^b - x_k^b - h_f f^b(u_k), \quad k = 0, 1, \dots, N_f - 1 \quad (32)$$

where Equation (31) approximates the solution of the storage temperature dynamics (22) using an implicit Euler integration scheme of order 1. Equation (32) for battery dynamics f^b is exact under the applied piecewise-constant control parameterization. The integral of the cost function (27) for the piecewise constant control for the k -th interval, is given by:

$$\int_{t_k}^{t_{k+1}} J_{\text{run}}(u(t)) = h_f J_{\text{run}}(u_k). \quad (33)$$

We can then summarize the transcribed continuous-time OCP (28) as the discretized NLP:

$$\begin{aligned} & \underset{\substack{x_{s,0}, \dots, x_{s,N_f}, \\ x_{b,0}, \dots, x_{b,N_f}, \\ u_0, \dots, u_{N_f-1}, \\ \theta}}{\text{minimize}} & \sum_{k=0}^{N_f-1} h_f \cdot J_{\text{run}}(u_k) + J_{\text{fix}}(\theta) \end{aligned} \quad (34a)$$

$$\text{subject to} \quad 0 = x_0^s - x_{N_f}^s, \quad (34b)$$

$$x_{k+1}^s = x_k^s + h_f f^s(x_{k+1}^s, u_k, t_k, \theta), \quad k = 0, \dots, N_f - 1, \quad (34c)$$

$$x_{\min}^s \leq x_k^s \leq x_{\max}^s \quad k = 0, \dots, N_f, \quad (34d)$$

$$0 = x_0^b - x_{N_f}^b, \quad (34e)$$

$$x_{k+1}^b = x_k^b + h_f f^b(u_k), \quad k = 0, \dots, N_f - 1, \quad (34f)$$

$$x_{\min}^b \leq x_k^b \leq x_{\max}^b \quad k = 0, \dots, N_f, \quad (34g)$$

$$0 \geq h(u_k, t_k, \theta) \quad k = 0, \dots, N_f - 1, \quad (34h)$$

$$0 = g(u_k, t_k, \theta) \quad k = 0, \dots, N_f - 1, \quad (34i)$$

$$u_{\min} \leq u_k \leq u_{\max} \quad k = 0, \dots, N_f - 1, \quad (34j)$$

$$\theta_{\min} \leq \theta \leq \theta_{\max} \quad (34k)$$

Here, the constraints are divided into groups: storage temperature states and controls (b-e), battery states and controls (f-i), and control/parameter constraints (j-l). The bounds on states and controls, as well as the (in)equalities g and h , are defined as described earlier.

4.1. Reduced-Size NLP Formulation using the Averaging Method

The previously formulated NLP involves hourly time steps across an entire year, resulting in 8760 discretization points. Even for relatively simple models, this high dimensionality presents significant challenges for solvers. However, seasonal thermal energy storage systems exhibit slowly varying temperature states $x(t)$ over hours or even days, despite rapid changes in

control input due to transient fluctuation of renewables or heat demand. Leveraging this observation, we average the storage temperature dynamics f^s (16) over a chosen time horizon T , one day. The averaged dynamics for the storage state $x^s(t)$ over the next single day $t \in [t_k, t_k + T]$ are defined as:

$$\bar{f}_k^s(x^s(t)) = \frac{1}{T} \int_{t_k}^{t_k+T} f^s(x^s(t), \tau) d\tau \quad (35)$$

where, the averaging duration $T = 1 \text{ d} = h_f K$, $K = 24$ is an integer multiple of the interval size h_f . This approach is justified using the Averaging Theorem, with further details provided in Appendix B.1.

The temperature dynamics f^s are dependent on the time t only via an affine dependence on the inputs $\dot{Q}_{\text{hp}}(t), \dot{Q}_{\text{load}}(t), T_{\text{amb}}(t)$, see Equation (17). Exploiting the linearity of the averaging operator, the day-averaged dynamics (35) for $t \in [t_k, t_k + T]$ become:

$$\bar{f}_k^s(x^s(t)) = \frac{1}{T} \int_{t_k}^{t_k+T} f^s(x^s(t), \tau) d\tau \quad (36)$$

$$= \frac{1}{T} \int_{t_k}^{t_k+T} f^s \left(x^s(t), \dot{Q}_{\text{hp}}(\tau), \dot{Q}_{\text{load}}(\tau), T_{\text{amb}}(\tau) \right) d\tau \quad (37)$$

$$= f^s \left(x^s(t), \bar{Q}_{\text{hp},k}, \bar{Q}_{\text{load},k}, \bar{T}_{\text{amb},k} \right) \quad (38)$$

where the values $\bar{Q}_{\text{hp},k}, \bar{Q}_{\text{load},k}, \bar{T}_{\text{amb},k}$, represent the day-averaged heat transfer rates and ambient temperature, respectively. The detailed calculations for these values can be found in Appendix B.2.

4.2. Modifying the NLP with the average temperature dynamics

We now separate the simulation of the averaged temperature dynamics and the fast battery dynamics. To address the differing timescales between the averaged temperature dynamics and the fast battery dynamics, we introduce a second, coarse grid with $N_c \ll N_f$ intervals, indexed by $j = 0, \dots, N_c$. This coarse grid is related to the fine grid via $k = j \cdot K$, $K = 24$, and is used to integrate the slow, average temperature dynamics with large steps of size $h_c = K \cdot h_f = 24 \text{ h}$. We choose the averaging window size to match the step size of the slow integration scheme, which is set to one day ($T = h_c$). This process is illustrated in Figure 5.

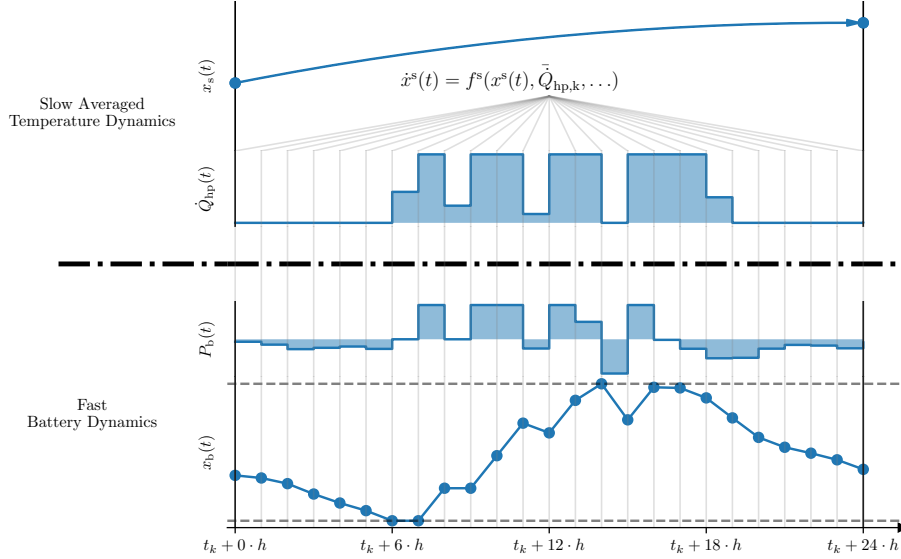


Figure 5: The average dynamics of the states x^s are integrated using coarse steps of size $h_c = 24$ h using the averaged inputs, while the fast battery dynamics are integrated over fine steps of $h_f = 1$ h to ensure constraint satisfaction.

The constraints and integration equations for the averaged temperature states on the coarse grid are:

$$0 = x_0^s - x_{N_c}^s \quad (39a)$$

$$x_{j+1}^s = x_j^s + h_c f^s \left(x_{j+1}^s, \bar{Q}_{hp,k}, \bar{Q}_{load,k}, \bar{T}_{amb,k} \right), \quad j = 0, \dots, N_c - 1 \quad (39b)$$

$$x_{\min}^s \leq x_j^s \leq x_{\max}^s, \quad j = 0, \dots, N_c \quad (39c)$$

where f^s is evaluated using an implicit Euler scheme with coarse step size h_c . The averaged inputs are calculated as in Equations (B.3), (B.4), and (B.7), with $k = jK$.

The modified NLP (34) is formulated as:

$$\begin{aligned} & \underset{\substack{x_{s,0}, \dots, x_{s,N_c}, \\ x_{b,0}, \dots, x_{b,N_f}, \\ u_0, \dots, u_{N_f-1}, \\ \theta}}{\text{minimize}} \quad (34a) & \quad \text{(Fine Grid Objective)} \quad (40a) \end{aligned}$$

$$\text{subject to} \quad (39) \quad \text{(Coarse Grid Constraints),} \quad (40b)$$

$$(34e)-(34g) \quad \text{(Fine Grid Constraints),} \quad (40c)$$

$$(34i)-(34k) \quad \text{(Control and Parameters Constraints)} \quad (40d)$$

This formulation reduces the number of NLP variables from $N_f \cdot (M + N + 1 + n_u) + n_\theta$ to $N_c \cdot (M + N) + N_f \cdot (1 + n_u) + n_\theta$, achieving a reduction of approximately 50% in the example presented later. Here, M and N represent the number of storage and ground layers, respectively. The separation of using different numerical methods for different timescales in the dynamics is consistent with prior works; we refer the reader to [21, 22, 23] and their references.

Other Implementation Details. We use CasAdi [24] to formulate the NLPs and solve them using IPOPT [25] with the linear solver MA27[26]. The initial temperatures of the storage and ground are set to 30 °C and 13.5 °C, respectively. All controls are initialized to zero, and scaling parameters are set to one. We scale the problem to ensure that all variables and their bounds are of order 1.

5. Results

In this section, we present a case study based on the system model and the optimal control problem (OCP) formulation.

We solve the optimization problem using hourly time series data for ambient temperature, electricity, heating demands, and relative renewable generation for 2023. The detailed power profiles for PV, wind generation in the Freiburg region, as well as heating load, are presented in Appendix A. Electricity demand is derived from the Energy Hub Design Optimization platform [9] and scaled to match the energy demand of the case study. Air temperature data is obtained from the German Meteorological Service (DWD) for the Freiburg station [27].

5.1. Economic Case Study: Dietenbach

This case study evaluates the feasibility of implementing a system with PTES in Dietenbach, a new district under construction in Freiburg, Germany². The development will house approximately 16 000 residents across 6 900 households, with an estimated annual heating demand of 51 GWh and electricity demand of 32 GWh [28]. Figure 6 shows the system’s weekly average demand.

²Ground conditions in Freiburg pose challenges for implementing PTES systems due to high groundwater flow speed [29], but the underlying principles are broadly applicable.

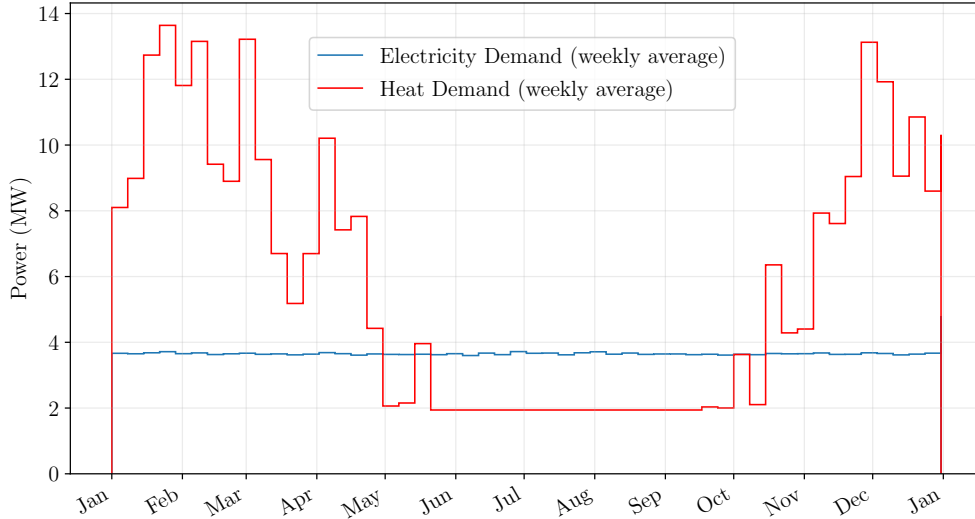


Figure 6: Weekly average of the demand

To evaluate the system, we solve the NLP (34) and determine the optimal design parameters, with the resulting sizes listed in the third column of Table 4. Figure 7 illustrates the optimal trajectories of the storage temperature dynamics. The top storage layer, $T_{s,1}$, is constrained to a minimum temperature of 40°C , enabling heat discharge until this limit is reached. The ground temperature, T_g , oscillates with the storage temperature, with the first layer being more affected by the storage than the second. The storage efficiency over the year is 94.4%.

Figure 8 illustrates grid usage in the system. The optimal strategy is to purchase electricity primarily in winter months when solar irradiation is insufficient, while excess electricity is fed into the grid during summer. The total amount of purchased and fed-in electricity are $E_{\text{grid,buy}} = 5.33 \text{ GWh}$ and $E_{\text{grid,feedin}} = 7.32 \text{ GWh}$, respectively.

5.1.1. Impact of Electricity Price Variations

Next, we analyze the impact of changes in electricity prices on the system. Starting with an initial price of 0.1 €/kWh , we increase $c_{\text{el,buy}}$ by 0.1 €/kWh increments, up to 1.0 €/kWh . To compare the scenarios, we introduce the metric “Autonomy”, defined as the ratio of renewable energy

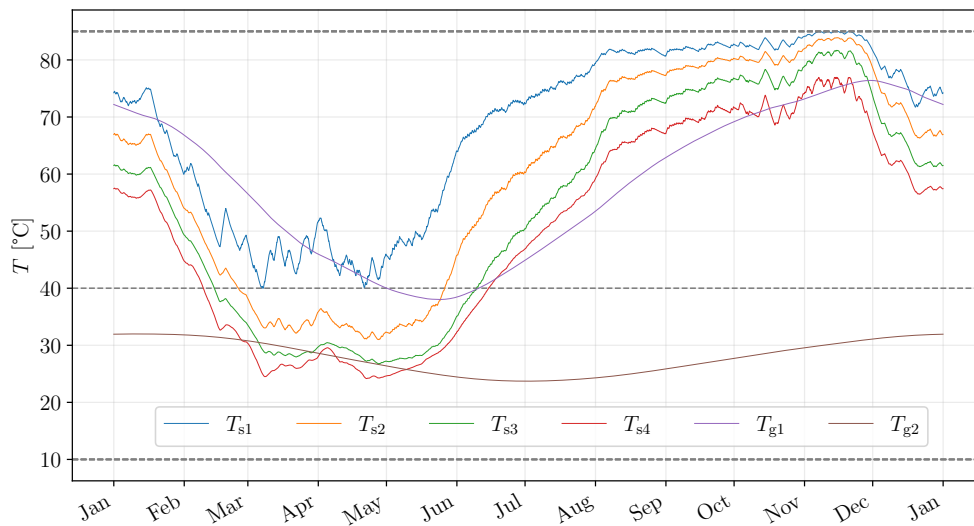


Figure 7: Optimal temperature trajectories

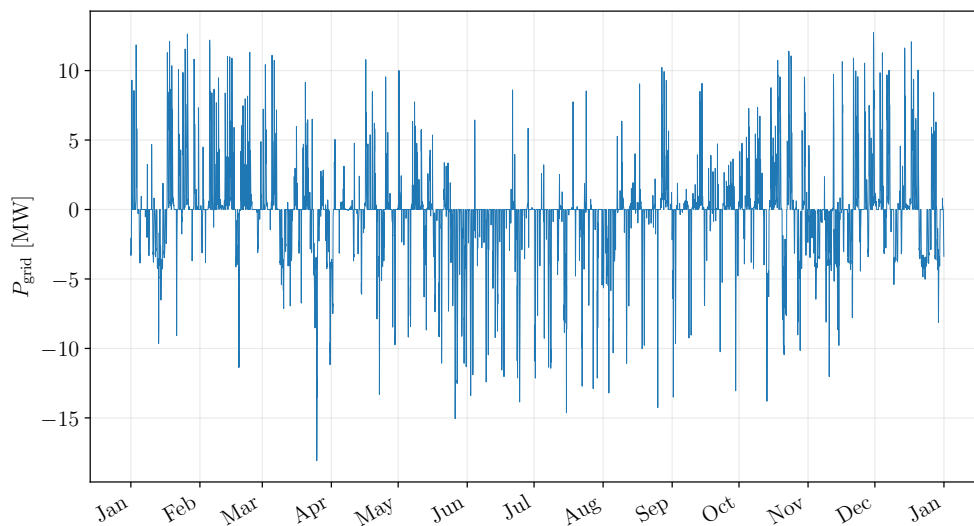


Figure 8: Optimal grid usage of the system

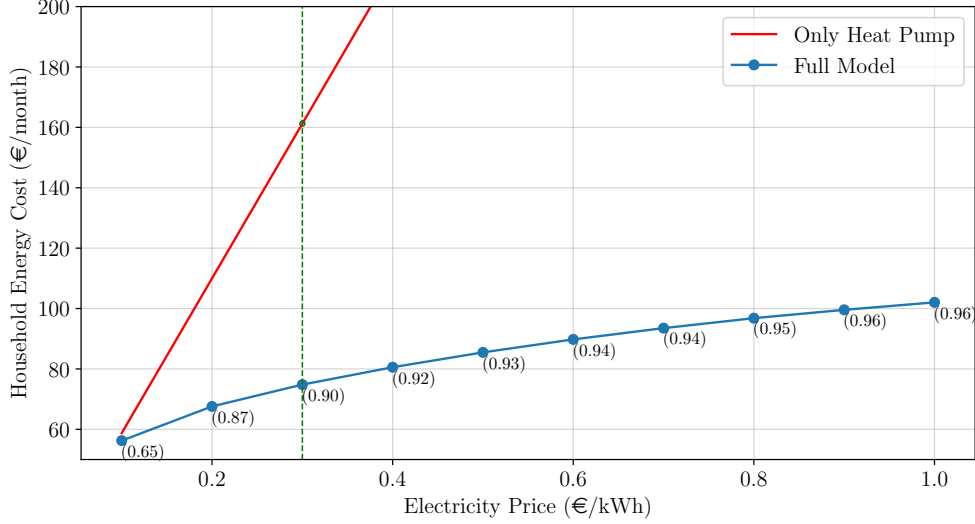


Figure 9: Cost comparison based on electricity price and autonomy level (in brackets)

generation to total electricity demand:

$$\text{Autonomy} := \frac{E_{\text{tot}} - E_{\text{grid,buy}}}{E_{\text{tot}}} \quad (41)$$

where,

$$E_{\text{tot}} = \int_0^{365d} (P_{\text{hp}}(t) + P_{\text{load}}(t)) dt \quad (42)$$

$$E_{\text{grid,buy}} = \int_0^{365d} P_{\text{grid}}^+(t) dt \quad (43)$$

As shown in Figure 9, increasing grid prices leads to higher total costs and greater autonomy, as indicated by the specific values in the plot. However, even with very high external electricity prices, achieving full autonomy remains challenging due to insufficient renewable generation during winter months, despite substantial investments in battery and renewable energy installations.

The total cost (TC) for a system relying solely on a heat pump can be expressed as:

$$\text{TC}_{\text{hp,only}} = c_{\text{el,buy}} \cdot E_{\text{hp,only}} + \text{CAPEX}_{\text{hp}} \cdot \text{ANF} + \text{OPEX}_{\text{hp}} \quad (44)$$

where $E_{\text{hp,only}}$ represents the total electricity consumption of the system with only a heat pump over a year:

$$E_{\text{hp,only}} = \int_0^{365\text{d}} (P_{\text{hp,only}}(t) + P_{\text{load}}(t)) dt \quad (45)$$

Here, the term $P_{\text{hp,only}}(t)$ denotes the instantaneous power consumption of the heat pump, calculated as:

$$P_{\text{hp,only}}(t) = \frac{\dot{Q}_{\text{load}}(t)}{\text{COP}_{\text{hp,only}}} \quad (46)$$

This model assumes the use of an air-source heat pump with an installed capacity of 20 MW to meet the peak heating demand. The system operates at a supply temperature of 40 °C, fulfilling the same district heating requirement. At realistic electricity prices, a system incorporating renewable energy proves to be far more cost-effective than one relying solely on a heat pump.

5.1.2. Role of Wind Generation in the Energy System

Figure 10 illustrates the optimized renewable generation, highlighting how PV and wind generation seasonally complement each other. To explore this interaction, we compare two scenarios: one with wind generation and one without. Table 4 summarizes the results.

Excluding wind generation increases the required capacities of PV, batteries, and thermal storage, indicating that wind generation mitigates the seasonality of PV production. Autonomy decreases by 7.1%, and total costs rise by 42.9% when wind generation is excluded. This demonstrates that wind power integration significantly aids in decarbonizing the energy system, even though wind generation may face economic or political challenges in some regions. Regardless of wind generation, incorporating heat storage and batteries offers clear economic and environmental advantages over a system with only a heat pump.

5.2. Numerical Study

By using Equation (40), the same optimal control problem can be solved with reduced time steps in the storage dynamics—365 steps for one year—while maintaining the same objective function and number of control variables. Figure 11 shows the optimal state trajectories of the averaged system compared to the original system. The dotted lines represent the averaged state

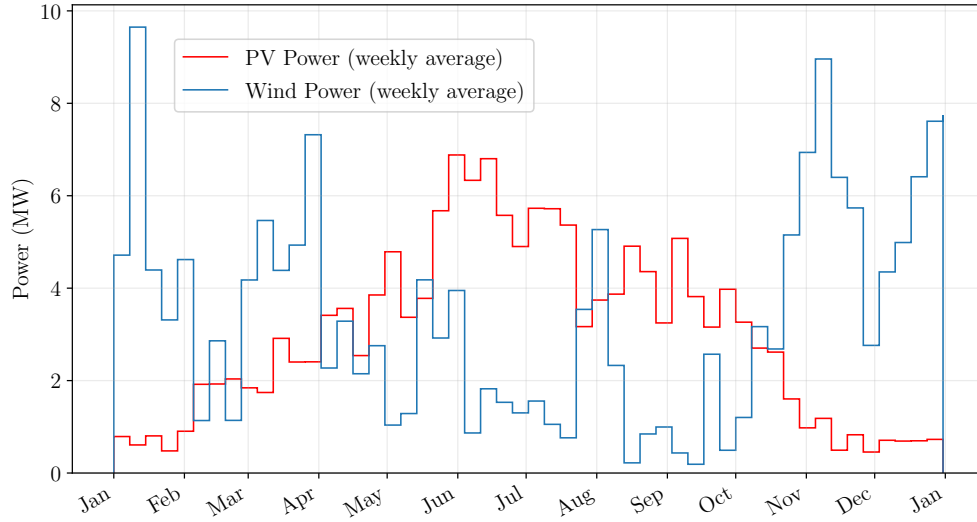


Figure 10: Weekly average of the renewable generation

Table 4: Comparison of the scenarios, $c_{el,buy} = 0.3 \text{ EUR/kWh}$

	Only HP	Full System	Without Wind	Unit
V_s	-	256 440	518 020	m^3
C_{hp}	20	15.18	30.78	MW_{th}
C_{pv}	-	21.01	41.70	MW_p
C_{wind}	-	12.64	-	MW_p
C_b	-	8.77	9.88	MWh
Autonomy	0	90.0	82.9	%
Total cost for 30 years	400.52	185.83	265.50	M€
Household energy cost	161.24	74.81	106.88	€/month

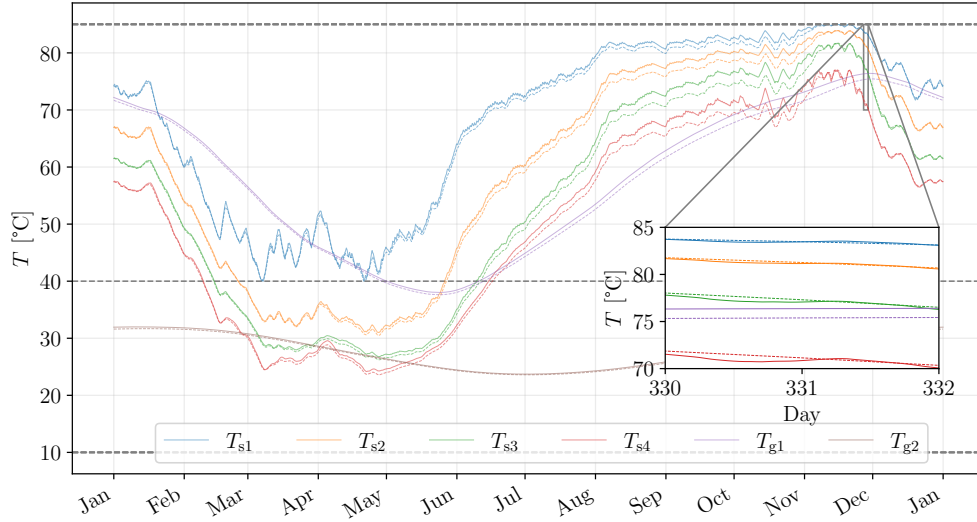


Figure 11: Comparison of the optimal temperature trajectories of the full NLP (34) and the averaged NLP (40).

Table 5: Comparison of the numerical solution of NLP (34) and NLP (40) regarding complexity and the performance

	Original Problem	Averaging Method	Unit
Total Variables	105 130	54 762	
Time per Iteration	0.581	0.122	s

dynamics, while the solid lines represent the original dynamics. The differences are barely visible, suggesting that the averaged state dynamics closely match the original system's. The Mean Absolute Percentage Error (MAPE) between the two approaches is only 0.2% while the computational time is significantly reduced. Table 5 compares the computational complexity and performance between the solution for the full NLP (34) and the NLP (40) employing the averaging method.

6. Conclusions

This work developed a mathematical model of a renewable energy system, including seasonal thermal energy storage (STES), a heat pump, a

battery, and the electricity grid. The underground storage system was modeled using a one-dimensional multi-node lumped-parameter method with uniform boundary conditions, incorporating temperature and mass flow dynamics in a stratified system. An optimization study based on these models yielded the following key findings:

1. **Real-world Case Study:** For the Dietenbach district in Freiburg, Germany, the proposed system achieved 90% self-sufficiency at a cost of 75€ per household per month, reducing costs by 53.6% compared to a system relying solely on heat pumps.
2. **Efficient Optimal Control:** The introduction of the averaging method reduced computation time by 79% while maintaining 99.8% accuracy.

These results emphasize the potential of STES in coupling electricity and heating sectors, highlighting its economic and environmental benefits in the context of increasing renewable energy use. However, certain assumptions—such as fixed electricity prices, single-year weather data, and fixed electricity and heat demand data—limit the generalizability of these findings. Additionally, the model excluded variations in geological conditions, groundwater flow, and thermal diffusivity for computational efficiency.

Future work could address uncertainties in weather data, integrate dynamic heat pump behavior, explore flexible storage layer use, and develop more detailed district heating network models. Additionally, utilizing sink temperature as a control variable and considering domestic hot water boosts could enhance system efficiency and cost-effectiveness.

Overall, this study contributes to the understanding of STES beyond traditional solar thermal applications, demonstrating its feasibility in real-world systems. It also advances research on optimal control for renewable energy systems and highlights the practical application of the averaging method.

Open Source Implementation

We provide the mini-toolbox for the code at <https://github.com/JakobHarz/NOSTES>

CRediT authorship contribution statement

Wonsun Song: Conceptualization, Methodology, Software, Validation, Formal analysis, Data curation, Writing – original draft, review & editing, Visualization. **Jakob Harzer:** Conceptualization, Methodology, Software, Validation, Writing – original draft, review & editing, Visualization. **Christopher Jung:** Data curation. **Leon Sander:** Data curation. **Moritz Diehl:** Conceptualization, Supervision.

Declaration of competing interest

The authors declare that they have no known competing financial interests or personal relationships that could have appeared to influence the work reported in this paper.

Acknowledgments

This research was supported by DFG via project 525018088, and by BMWK via 03EN3054B. We thank Manuel Kollmar, Armin Nurkanović, Dirk Schindler, and Arne Groß for their help, guidance, and fruitful discussions.

Appendix A. Modeling Details

Appendix A.1. Photovoltaics Model

The hourly solar PV module power output is calculated based on hourly-averaged solar radiation and air temperature time series obtained from the German Meteorological Service (DWD) for the Freiburg station [27]. The calculation follows the methods described by [30, 31] and uses parameters from the modern PV module type Longi Hi-Mo X6 Scientist LR5-72 HTH 590-600 M [32]. This module has an electrical efficiency of 23.2% and a temperature coefficient of $-0.290\%/^{\circ}\text{C}$. We assume that the PV module is tilted at an angle of 30° towards the south, with global horizontal irradiance (GHI) adjusted by dividing by $\cos(30^{\circ})$ [33].

Appendix A.2. Wind Model

The wind turbine power output is estimated using hourly wind speed data simulated at a height of 166 m from the Wind speed Complementarity (WiCoMo) model [34] and the power curve of a 5.6 MW wind turbine. Although the model accounts for integer numbers of turbines, the power output is scaled by s_{wind} to represent fractional installed capacities for the optimization study.

Appendix A.3. Heating Load Model

The heating demand is divided into space heating (SH) and domestic hot water (DHW) heating. For space heating, we use a simplified model that incorporates the effective temperature, T_{eff} , calculated as the 1-day moving average of T_{amb} :

$$T_{\text{eff}}(t) = \frac{1}{1\text{d}} \int_{t-1\text{d}}^t T_{\text{amb}}(\tau) d\tau. \quad (\text{A.1})$$

Heating is supplied when $T_{\text{eff}}(t)$ falls below the threshold temperature, $T_{\text{border}} = 12^\circ\text{C}$. The heating demand depends on the temperature difference between the room temperature $T_{\text{room}} = 20^\circ\text{C}$ and $T_{\text{eff}}(t)$. The space heating demand is scaled by the factor s_{sh} , resulting in a total space heating demand of 34 GWh. This relationship is expressed as:

$$\dot{Q}_{\text{sh}}(T_{\text{eff}}(t)) = \begin{cases} 0, & \text{if } T_{\text{eff}}(t) \geq T_{\text{border}}, \\ s_{\text{sh}} \cdot (T_{\text{room}} - T_{\text{eff}}(t)), & \text{if } T_{\text{eff}}(t) < T_{\text{border}}. \end{cases} \quad (\text{A.2})$$

The domestic hot water demand, \dot{Q}_{dhw} , is modeled with daily peak usage in the morning and evening. These peaks are represented by Gaussian functions:

$$\dot{Q}_{\text{dhw}}(t) = s_{\text{dhw}} \cdot (\dot{Q}_{\text{morning}}(t) + \dot{Q}_{\text{evening}}(t)), \quad (\text{A.3})$$

where $\dot{Q}_{\text{morning}}(t)$ and $\dot{Q}_{\text{evening}}(t)$ are defined as:

$$\dot{Q}(t) = \exp\left(-\frac{(t - \mu)^2}{2\sigma^2}\right), \quad (\text{A.4})$$

with μ and σ representing the mean and standard deviation of the peak demand, respectively. The demand is scaled by s_{dhw} , for 17 GWh for our case study.

Finally, the total heating demand, $\dot{Q}_{\text{load}}(t)$, is the sum of the space heating and domestic hot water demands, 51 GWh:

$$\dot{Q}_{\text{load}}(t) = \dot{Q}_{\text{sh}}(t) + \dot{Q}_{\text{dhw}}(t). \quad (\text{A.5})$$

Appendix A.4. Underground Thermal Energy Storage Model

When modeling underground thermal energy storage using the multi-node lumped-parameter method, the key considerations are the number of

layers and the distance between the storage and the ground. Both factors significantly influence the model accuracy: increasing the number of layers and the distance improves accuracy but adds complexity. For computational efficiency, the experiments in this section employ a fully mixed storage model, which assumes only one temperature node for the storage.

We treat the number of layers, n , and the distance, d , as parameters. The resulting storage temperature, $T_s(n, d)$, depends on both n and d . To evaluate the accuracy of the model, we define the ground truth \tilde{T}_s , using $n = 500$ layers and a distance of $d = 100$ m. Based on this ground truth, we calculate the error norm of $T_s(n, d)$ over a one-year simulation with N_f discretization intervals. Since the numerical error increases with larger values, we apply a logarithmic transformation using \log_{10} and use the Root Mean Square Logarithmic Error (RMSLE) to assess the model's accuracy. RMSLE is defined as:

$$\text{RMSLE} = \sqrt{\frac{1}{N_f} \sum_{i=1}^{N_f} \left(\log_{10}(T_s(n, d)) - \log_{10}(\tilde{T}_s) \right)^2} \quad (\text{A.6})$$

Figure A.12 shows the simulation results for different models. As expected, increasing the number of layers and distance leads to higher accuracy, closely approximating \tilde{T}_s . However, to balance computational efficiency and accuracy, we choose a model with $n = 2$ layers and a distance of 4 m, as indicated by the red cross in Figure A.12. This model already achieves good accuracy with an RMSLE of $0.5 \cdot 10^{-3}$.

Appendix B. Averaging Method

Appendix B.1. Theory of the Averaging Method

We motivate using the average dynamics by the following theorem, adapted from [35] (Lemma 2.1.8),

Lemma 1 (Averaging Theorem). *Consider the solution $x(t)$ of the initial value problem*

$$\dot{x}(t) = \epsilon f(x(t), t), \quad x(0) = a \quad (\text{B.1})$$

where the dynamics $f^1 : \mathbb{R}^{n_x} \times \mathbb{R}$ are Lipschitz continuous in (x, t) and T -periodic in t , and $0 < \epsilon \ll 1$. Then, the solution $y(t)$ of the averaged

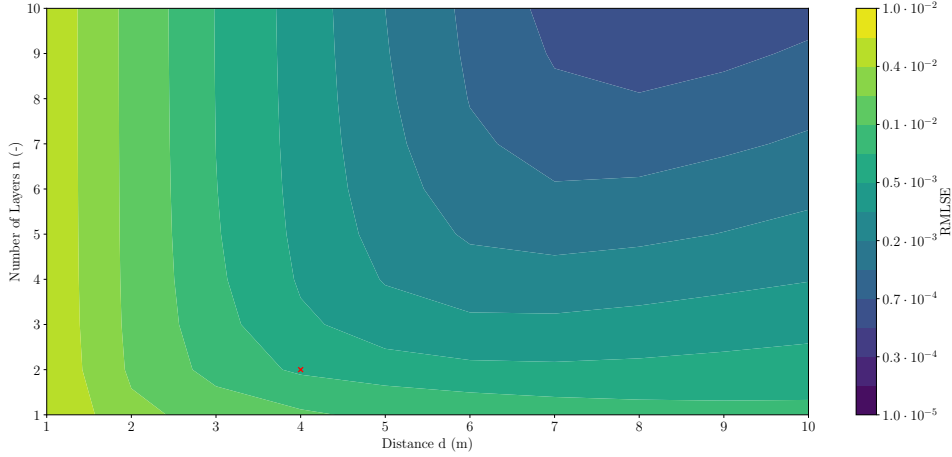


Figure A.12: Simulation results for fully mixed underground storage models with different n and d

dynamics

$$\dot{y}(t) = \epsilon \bar{f}(y(t)) = \epsilon \int_0^T f(y(t), \tau) d\tau \quad (\text{B.2})$$

with initial value $y(0) = a$ approximates the solution of the original dynamics as $y(t) = x(t) + \mathcal{O}(\epsilon)$ on the timescale $1/\epsilon$.

For proof and more details, we refer the reader to [35]. Some remarks are in order. First of all, the temperature dynamics f^s (Equation (16)) are of the particular form ϵf where the parameter ϵ is equivalent to the inverse of the thermal capacity of the smallest discretization volume. Secondly, the dynamics $f^s(x, t)$ are not 1-periodic, but since we only compute the average dynamics for a particular day, we can consider the time-dependence to be periodic as $f_k^s(x^s, t) = f^s(x^s, t_k + (t \bmod T))$. Third, since we apply the controls and time series for the ambient temperature and heat transfer rates as piecewise constant over the intervals, the dynamics f_s are not Lipschitz continuous in t . Thus, to strictly satisfy the conditions of the above Lemma, a different (continuous) parametrization would be required. However, the averaging of the dynamics with a piecewise constant parametrization, despite not being Lipschitz in t , provides good approximations, as shown by our comparisons. Extending the theory of the averaging method to piecewise constant control is a potential subject for future research.

Appendix B.2. Calculation Details for the Averaging Method

The day-averaged values of $\dot{Q}_{\text{load}}(t)$ and $T_{\text{amb}}(t)$ are calculated as single sums, due to the piecewise constant parameterization and the averaging horizon T being integer multiples of the step size h_f , given by:

$$\bar{\dot{Q}}_{\text{load},k} := \frac{1}{T} \int_{t_k}^{t_k+T} \dot{Q}_{\text{load}}(t) dt = \frac{1}{K} \sum_{i=k}^{i=k+K-1} \dot{Q}_{\text{load},i} \quad (\text{B.3})$$

$$\bar{T}_{\text{amb},k} := \frac{1}{T} \int_{t_k}^{t_k+T} T_{\text{amb}}(t) dt = \frac{1}{K} \sum_{i=k}^{i=k+K-1} T_{\text{amb},i}. \quad (\text{B.4})$$

For $\dot{Q}_{\text{hp}}(t)$, averaging requires careful consideration of its non-linear dependence on T_{amb} . It is given by:

$$\bar{\dot{Q}}_{\text{hp},k} := \frac{1}{T} \int_0^T \dot{Q}_{\text{hp}}(t) dt \quad (\text{B.5})$$

$$= \frac{1}{T} \int_0^T \eta_{\text{Lorenz}} \cdot \frac{T_{\text{hp}}}{T_{\text{hp}} - T_{\text{amb}}(t)} \cdot P_{\text{hp}}(t) dt \quad (\text{B.6})$$

$$= \frac{1}{K} \sum_{i=k}^{i=k+K-1} \eta_{\text{Lorenz}} \cdot \frac{T_{\text{hp}}}{T_{\text{hp}} - T_{\text{amb},i}} \cdot P_{\text{hp},i} \quad (\text{B.7})$$

Here, the term $\eta_{\text{Lorenz}} \cdot \frac{T_{\text{hp}}}{T_{\text{hp}} - T_{\text{amb},i}}$ represents time-dependent but fixed problem data, while $P_{\text{hp},i}$ is optimization variable.

References

- [1] IEA, World energy outlook 2023 (2023).
- [2] International Renewable Energy Agency, Green Hydrogen Cost Reduction: Scaling up Electrolysers to Meet the 1.5°C Climate Goal (2020).
- [3] Kallesøe, A.J. & Vangkilde-Pedersen, T., Underground Thermal Energy Storage (UTES) – state-of-the-art, example cases and lessons learned. HEATSTORE project report, GEOTHERMICA – ERA NET Cofund Geothermal. (2019).
- [4] C. Multiphysics, Introduction to comsol multiphysics®, COMSOL Multiphysics, Burlington, MA 9 (1998) 2018.
- [5] S. Klein, et al., TRNSYS 18: A Transient System Simulation Program, Solar Energy Laboratory, University of Wisconsin, Madison, USA, 2017.
- [6] A. Dahash, F. Ochs, A. Tosatto, W. Streicher, Toward efficient numerical modeling and analysis of large-scale thermal energy storage for renewable district heating, Applied Energy 279 (2020) 115840. doi:10.1016/j.apenergy.2020.115840.

- [7] F. Ochs, A. Dahash, A. Tosatto, M. Reisenbichler, K. O’Donovan, G. Gauthier, C. K. Skov, T. Schmidt, Comprehensive comparison of different models for large-scale thermal energy storage, in: Proceedings of the International Renewable Energy Storage Conference 2021 (IRES 2021), Atlantis Press, 2022, pp. 36–51. doi:10.2991/ahe.k.220301.005.
URL <https://doi.org/10.2991/ahe.k.220301.005>
- [8] L. Kotzur, P. Markewitz, M. Robinius, D. Stolten, Time series aggregation for energy system design: Modeling seasonal storage, Applied Energy 213 (2018) 123–135. doi:10.1016/j.apenergy.2018.01.023.
- [9] M. Wirtz, P. Remmen, D. Müller, EHDO: A free and open-source webtool for designing and optimizing multi-energy systems based on MILP, Computer Applications in Engineering Education 29 (5) (2021) 983–993. doi:10.1002/cae.22352.
- [10] L. T. Biegler, Nonlinear programming: concepts, algorithms, and applications to chemical processes, SIAM, 2010.
- [11] J. B. Rawlings, D. Q. Mayne, M. M. Diehl, Model Predictive Control: Theory, Computation, and Design, 2nd Edition, Nob Hill, 2017.
- [12] J. T. Betts, Practical Methods for Optimal Control and Estimation Using Nonlinear Programming, Second Edition, 2nd Edition, Society for Industrial and Applied Mathematics, 2010. doi:10.1137/1.9780898718577.
- [13] H. Fontenot, B. Dong, Modeling and control of building-integrated microgrids for optimal energy management – a review, Applied Energy 254 (2019) 113689. doi:10.1016/j.apenergy.2019.113689.
- [14] F. Schlosser, M. Jesper, J. Vogelsang, T. G. Walmsley, C. Arpagaus, J. Hesselbach, Large-scale heat pumps: Applications, performance, economic feasibility and industrial integration, Renewable and Sustainable Energy Reviews 133 (2020) 110219. doi:10.1016/j.rser.2020.110219.
- [15] M. De Carli, M. Tonon, A. Zarrella, R. Zecchin, A computational capacity resistance model (CaRM) for vertical ground-coupled heat exchangers, Renewable Energy 35 (7) (2010) 1537–1550, special Section: IST National Conference 2009. doi:10.1016/j.renene.2009.11.034.
- [16] T. Ommen, W. B. Markussen, B. Elmegaard, Lowering district heating temperatures – impact to system performance in current and future danish energy scenarios, Energy 94 (2016) 273–291. doi:10.1016/j.energy.2015.10.063.
- [17] U. Eicker, Solar Technologies for Buildings, John Wiley & Sons, 2003.
- [18] NREL (National Renewable Energy Laboratory), 2024 Annual Technology Baseline, <https://atb.nrel.gov/electricity/2024/index>, (accessed December 19, 2024) (2024).
- [19] I. Sifnaios, D. M. Sneum, A. R. Jensen, J. Fan, R. Bramstoft, The impact of large-scale thermal energy storage in the energy system, Applied Energy 349 (2023) 121663. doi:10.1016/j.apenergy.2023.121663.
- [20] S. Wolf, R. Flatau, P. Radgen, M. Blesl, Systematische Anwendung von Großwärmepumpen in der Schweizer Industrie (in German), <https://www.bfe.admin.ch/bfe/de/home/versorgung/energieeffizienz/umgebungswaerme.html>, (accessed December 20, 2024) (2017).
- [21] P. Williams, Optimal control of electrodynamic tether orbit transfers using timescale separation, Journal of Guidance, Control, and Dynamics 33 (1) (2010) 88–98.

- [22] C.-J. Kim, S. Sung, S. H. Park, S. N. Jung, T. S. Park, Numerical time-scale separation for rotorcraft nonlinear optimal control analyses, *Journal of Guidance, Control, and Dynamics* 37 (2) (2014) 658–673. doi:10.2514/1.59557.
- [23] Y. Lishkova, S. Ober-Blöbaum, M. Cannon, S. Leyendecker, A multirate variational approach to simulation and optimal control for flexible spacecraft, arXiv preprint arXiv:2009.05873 (2020).
- [24] J. A. E. Andersson, J. Gillis, G. Horn, J. B. Rawlings, M. Diehl, Casadi - a software framework for nonlinear optimization and optimal control, *Mathematical Programming Computation* 11 (1) (2019) 1–36. doi:10.1007/s12532-018-0139-4.
- [25] A. Wächter, L. Biegler, On the implementation of an interior-point filter line-search algorithm for large-scale nonlinear programming, *Mathematical Programming* 106 (2006) 25–57. doi:10.1007/s10107-004-0559-y.
- [26] HSL, A collection of Fortran codes for large scale scientific computation, <http://www.hsl.rl.ac.uk>, (accessed December 20, 2024) (2011).
- [27] Deutscher Wetterdienst, Climate data for direct download, https://www.dwd.de/EN/ourservices/cdc/cdc_ueberblick-klimadaten_en.html, (accessed December 19, 2024) (2024).
- [28] T. Nusser, M. Stickel, S. Idler, Energiekonzept für den neuen Stadtteil Dietenbach im Auftrag der Stadt Freiburg (in German), <https://www.freiburg.de/pb/1733405.html> (2021).
- [29] R. Stemmler, H. Lee, P. Blum, K. Menberg, City-scale heating and cooling with aquifer thermal energy storage (ATES), *Geothermal Energy* 12 (1) (2024). doi:10.1186/s40517-023-00279-x.
- [30] L. Sander, C. Jung, D. Schindler, New concept of renewable energy priority zones for efficient onshore wind and solar expansion, *Energy Conversion and Management* 294 (2023) 117575. doi:10.1016/j.enconman.2023.117575.
- [31] L. Sander, D. Schindler, C. Jung, Application of satellite data for estimating rooftop solar photovoltaic potential, *Remote Sensing* 16 (12) (2024) 2205. doi:10.3390/rs16122205.
- [32] Longi, Longi Hi-Mo X6 Scientist LR5-72 HTH 590-600 M, https://static.longi.com/L_Gi_LE_PM_T_PMD_059_F133_LR_5_72_HTH_590_600_M_35_35_and_15_Frame_Scientist_V19_fa84b95a79.pdf, (accessed December 19, 2024) (2024).
- [33] Z. Sen, *Solar energy fundamentals and modeling techniques: atmosphere, environment, climate change and renewable energy*, Springer Science & Business Media, 2008.
- [34] C. Jung, D. Schindler, Introducing a new wind speed complementarity model, *Energy* 265 (2023) 126284. doi:10.1016/j.energy.2022.126284.
- [35] J. A. Sanders, F. Verhulst, J. A. Murdock, Averaging methods in nonlinear dynamical systems, 2nd Edition, Vol. 59 of Applied mathematical sciences (Springer-Verlag New York Inc.), Springer, New York, 2007.